nature catalysis

Article

https://doi.org/10.1038/s41929-024-01162-z

Modulating water hydrogen bonding within a non-aqueous environment controls its reactivity in electrochemical transformations

Received: 11 July 2023

Accepted: 11 April 2024

Published online: 24 May 2024

Check for updates

Reginaldo J. Gomes ♠, Ritesh Kumar ♠, Hannah Fejzić ♠, Bidushi Sarkar ♠, Ishaan Roy ♠ & Chibueze V. Amanchukwu ♠ 🖂

Electrochemical carbon dioxide reduction (CO_2R) can provide a sustainable route to produce fuels and chemicals; however, CO_2R selectivity is frequently impaired by the competing hydrogen evolution reaction (HER), even for small concentrations of water. Here we tune water solvation and dynamics within a series of aprotic solvents featuring different functional groups and physicochemical properties to modulate HER activity and CO_2R selectivity. We show that one can extend the HER onset potential by almost 1 V by confining water within a strong hydrogen bond network. We then achieve nearly 100% CO Faradaic efficiency at water concentrations as high as 3 M with a gold catalyst. Furthermore, under mildly acidic conditions, we sustain nearly 100% Faradaic efficiency towards CO with no carbonate losses over long-term electrolysis with an earth-abundant zinc catalyst. Our work provides insights to control water's reactivity and reveals descriptors to guide electrolyte design for important electrochemical transformations.

Water plays a pivotal role in this century's energy transition in the same way it has done in the past (hydroelectric, steam engine and so on). Next-generation electrochemical-based technologies such as water electrolysis, aqueous batteries and low-temperature CO_2 conversion all have unique water needs. To produce hydrogen through water electrolysis, higher water electrochemical activity is needed to decrease the overall cell overpotential. By contrast, suppression of water activity is needed for aqueous batteries to operate over a wider electrochemical potential range². For CO_2 reduction (CO_2R), there is an intermediate need: water activity needs to be modulated such that water can act favourably as a proton donor to yield chemicals and fuels³, while not participating in undesired hydrogen evolution reaction (HER)⁴. The successful deployment of low-carbon electrochemical technologies is thus dependent on modulating water's properties and its electrochemical activity.

Water's ability to form multiple hydrogen bonds (HBs) with neighbouring molecules plays a dominant role in its electrochemical

properties. The HB dynamics of water during the HER have been probed through multiple in situ techniques and molecular dynamics (MD) calculations⁵⁻⁹. Recent efforts have focused on modulating the HB strength and dynamics to either enhance or completely suppress HER activity. In a seminal work on aqueous batteries by Suo et al.¹⁰, high salt concentrations (typically greater than 20 mol kg⁻¹) were used to increase the water electrochemical window from its thermodynamic limit (1.23 V) to around 3 V. In this regime, water molecules are mostly present within the first solvation shell around cations and anions, restricting water reorientation dynamics¹¹ and enhancing electrochemical stability. This approach has been widely explored for numerous aqueous battery chemistries¹² but the high viscosity and electrolyte cost (the salt is the most expensive component of an electrolyte) have led to other approaches.

Molecular crowding agents such as polyethylene glycol¹³ and common organic molecules such as dimethyl sulfoxide (DMSO)¹⁴,

Pritzker School of Molecular Engineering, The University of Chicago, Chicago, IL, USA. Se-mail: chibueze@uchicago.edu

sulfolane¹⁵ and caprolactams¹⁶ can also form strong HBs with water and suppress HER activity. Although these advances have primarily been for aqueous batteries, it is still an incipient field for other relevant electrocatalytic transformations. For CO_2R , there is a great need to suppress the HER, as the selectivity towards carbon-containing products is a sensitive variable for its techno-economic feasibility^{17,18}. The use of an aprotic medium (no ionizable protons) has also been a promising strategy to suppress HER and increase CO_2R selectivity. However, maintaining a completely dry non-aqueous electrolyte is technically challenging because the solvents and salts are hygroscopic and thus even small amounts of water (<0.1 M) can lead to Faradaic efficiency (FE) values for H_2 of around 20% in solvents such as propylene carbonate (PC) and acetonitrile (ACN)^{19,20} Therefore, using insights from aqueous batteries, we hypothesize that controlling water–solvent interactions provides a pathway to modulating water activity and reactivity.

Despite the need to suppress the HER, the addition of water can also promote an increase in CO₂R activity in a non-aqueous medium. In our current understanding, water molecules present at the electrode surface can facilitate proton-coupled electrochemical reactions that take place during the CO₂R and may stabilize certain intermediates²¹. Nevertheless, this promoting effect is also accompanied by an increase in HER activity. Dubouis et al.²² have recently shown that by creating HB interactions between water molecules at short range (for example, at high water content), small water clusters are formed in ACN, leading to lower overpotentials for the HER. Another important challenge associated with water addition is the electrolyte depletion through carbonate formation^{23–25}. During CO₂ reduction, the electrolyte pH increases due to the in situ generated OH⁻ from both the CO₂R and parasitic HER. The resulting alkaline medium leads to continuous consumption of CO₂ through carbonate formation, increasing the costs for CO₂ recovery²⁶. Therefore, it is of paramount interest to develop new electrolytes that can lower CO₂R overpotentials, while preventing a parasitic HER and carbonate formation.

In this work we investigate the effect of solvent-water interactions on HER activity and CO₂R selectivity. We added water to a series of organic aprotic solvents featuring different functional groups and physicochemical properties. Using extensive spectroscopic analyses, we show that the HB strength increases with solvent donor number. Importantly, our density functional theory (DFT) calculations and MD simulations show that it is not just the amount of free water that necessarily correlates with HER activity, but also the HB strength and the cooperative effect induced by the solvent on water-water dynamics. We then explore the influence of these bulk solvation changes on CO₂R selectivity. Using a gold electrode, we show that confining water molecules within a stronger HB network (high donor number solvent) allows for the total suppression of HER with an almost 100% CO FE while lowering CO₂R overpotentials by ~140 mV. These insights are then exploited in a mildly acidic medium to prevent CO₂ losses from carbonate formation. As proton reduction happens at less negative potentials than water reduction, CO₂R selectivity in an acidic medium is further plagued by the HER²⁷. However, by using a strong HB donor solvent such as DMSO, we obtain 98 ± 3% FE values with gold and an earth-abundant zinc catalyst, with virtually no carbonate losses. Our work broadens our understanding of modulating and controlling water activity for a wide range of electrocatalytic systems.

Results

Water-solvent interactions

The influence of the aprotic solvent (Fig. 1a) nature on the water microenvironment was probed using different spectroscopic techniques. A mixture of 1 M H_2O in D_2O was used to better illustrate the common solvation structures observed for liquid water at room temperature through the infrared (IR) spectroscopy technique. As shown in Fig. 1b, liquid water exhibits a broad peak centred around 3,300 cm⁻¹, which is ascribed to strong HB networks comprising multiple water molecules

with single hydrogen donors^{28–32}. The peak centred at 3,430 cm⁻¹ is assigned to multiple water molecules forming HBs with double hydrogen donors^{31,32}, whereas the peak at 3,550 cm⁻¹ is ascribed to a weaker HB network composed of water dimers and trimers with one hydrogen donor^{33,34}. A narrower peak around 3,650 cm⁻¹ is associated with non-coordinated or free water molecules^{35,36}. An illustration of the different water HB networks is shown in Fig. 1c.

Figure 1d shows the O-H stretching modes for water in different aprotic solvents. We intentionally chose a relatively low water concentration (1 M) to amplify the influence of the solvent's characteristics on the solvent-H₂O interactions. Nevertheless, this concentration is still relevant for electrochemical applications (refer to Supplementary Fig. 1 for the complete IR spectra for all of the solvents). From Fig. 1d, we observe new peaks that arise from the different HB networks involving solvent-H₂O interactions. For water in dimethylsulfoxide (DMSO) and dimethylformamide (DMF), most of the peak's distribution is located between 3,200 and 3,500 $\mathrm{cm^{-1}}$ – a region similar to the strong HB networks found in the water molecules in D₂O. A considerable blue shift towards frequencies greater than 3,600 cm⁻¹ is observed for water in ACN and PC. This region is also characteristic of the stretching frequency of free O-H groups present in the solvation shell of hydrophobic molecules, also called dangling O-H groups³⁷⁻³⁹. Water present in 1,2 dimethoxyethane (DME), sulfolane (SUL) and tetrahydrofuran (THF) exhibit an HB network of moderate strength. Finally, we can observe an increase in the percentage of free water moving from DMS O < DMF < THF < DME < SUL < ACN < PC. Similar trends for free water and HB strength were also observed in the O-H Raman shift for water in different solvent mixtures (Supplementary Fig. 2).

The strength of the water HBs in different solvents was then investigated. It has been shown that dilute isotopes can be used as a vibrational probe for the water HB environment (for example, by diluting H_2O in D_2O or vice versa) 29,40 . According to our current understanding, strong HBs will result in less polarized O–H bonds and a consequent red-shift in their frequency. By contrast, weaker HBs will lead to a blue shift 29,41 . Figure 1e shows the O–H stretching regions for HOD solutions in different aprotic solvents. Similar to the trends observed for H_2O IR results, we observed that DMSO and DMF presented a more red-shifted O–H stretching frequency, followed by THF, DME, SUL, PC and ACN, respectively. Those results indicate that DMSO and DMF present a stronger water HB when compared with the other solvents, whereas ACN and PC exhibit the weakest.

We conducted ¹H NMR experiments to probe further the effect of the solvent–H₂O interactions on the HB network strength. The NMR spectra for all solvents are shown in Supplementary Fig. 2b. From the water ¹H chemical shift shown in Fig. 1f, we observed more upfield chemical shifts for ACN and PC, but more downfield chemical shifts for DMF and DMSO. It has been shown ^{42–44} that when a hydrogen atom participates in an HB, its isotropic ¹H nuclear magnetic shielding constantly shifts downfield. This increase in resonating frequency is associated with a stronger HB, which contributes to the electronic deshielding of the proton. Our ¹H chemical shifts are therefore in alignment with what we observed for the water HOD stretching frequency; water forms stronger HB networks in DMF and DMSO, but weaker ones in ACN and PC.

Our spectroscopic studies collectively revealed that the water HB network strength is a function of its microenvironment. We therefore correlated the different physical and chemical properties of aprotic solvents (Supplementary Table 1) with the observed changes in the percentage of free water, HOD stretching frequency and ¹H chemical shifts (Supplementary Fig. 3). Among them, Gutmann's donor number presents a linear correlation with our spectroscopic results, as shown in Fig. 1g. The donor number empirical scale quantifies the electron-donating property of a solvent molecule⁴⁵. For all of the aprotic solvents investigated here, the dominant form of HB interactions is through the electron lone pair from their oxygen or nitrogen

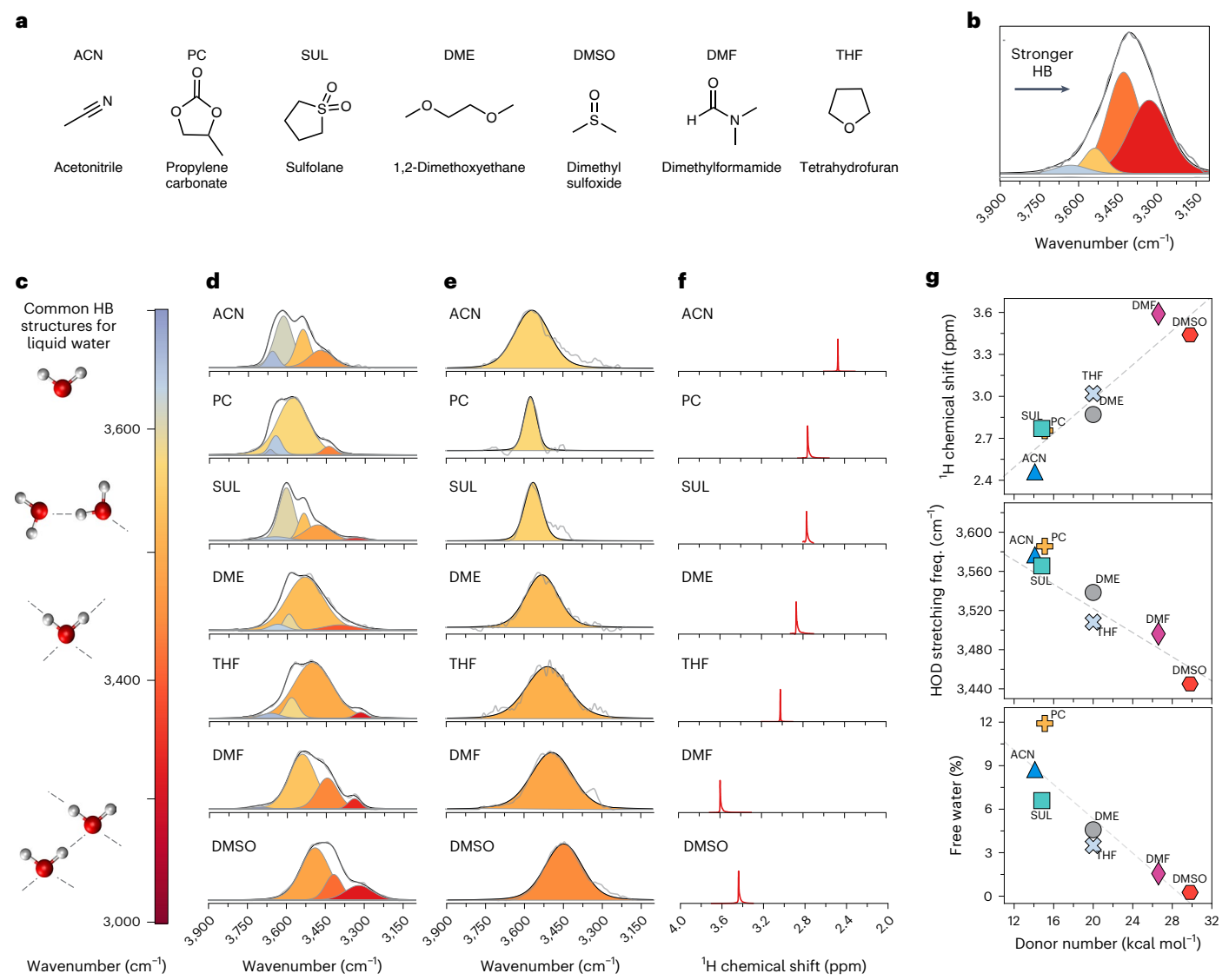


Fig. 1 | **Water speciation in organic media. a**, Chemical structures of different aprotic solvents studied in this work. **b**, Infrared spectra of $1 \, \text{MH}_2 \text{O}$ in $\text{D}_2 \text{O}$. **c**, Illustration of typical HB structures reported for liquid water at room temperature. **d**, IR spectra of water in different solvent mixtures ($1 \, \text{MH}_2 \text{O}$). **e**, IR spectra of the HOD stretching region for water in different solvent mixtures

containing 1 M water composed of 85% D_2O and 15% H_2O (v/v). \mathbf{f} , 1H NMR chemical shifts for water in different solvent mixtures (1 M H_2O). Peaks highlighted red correspond to the water peaks. \mathbf{g} , Correlation between solvent donor number and percentage of free water, HOD stretching frequency and 1H chemical shift extracted from \mathbf{d} , \mathbf{e} and \mathbf{f} , respectively. Dashed lines are to guide the eyes.

atoms. It is therefore not surprising that a metric for solvent basicity could be correlated with its effect on the water HB network strength. A similar correlation can also be observed for the solvent Kamlet–Taft HB accepting ability (β) in Supplementary Fig. 3.

We next used classical MD simulations and DFT calculations to elucidate our spectroscopic results, and further investigate the water solvation and dynamics in the presence of aprotic solvents (see Supplementary Note 1 and Supplementary Table 2 for more details). Figure 2a illustrates the primary solvation sheath around a typical water molecule, composed of either solvent and/or other water molecules within 3.1 Å from the water oxygen centre 46. This value corresponds to the characteristic water HB length at room temperature. We may also have non-coordinating or free water, where neither solvent nor other water molecules are present within the HB characteristic length.

We then established correlations between the simulated water properties and the observed IR results (similar correlations for NMR results can be found in Supplementary Fig. 4). Figure 2b shows a correlation between the experimentally obtained HOD average

stretching frequency and the simulated distribution of solvent-free water. These results indicate that about half of the water molecules are either free, or in the form of clusters, when dissolved in ACN and PC, resulting in a higher O–H stretching frequency. In contrast, the distribution of solvent-free water decreases as we observe a red-shift in the O–H frequency, reaching values close to 0% for DMSO. Those results are also in agreement with the percentage of free water extracted from the IR data (Supplementary Fig. 5). A clear picture of the water solvation structures in some selected solvents is illustrated in Fig. 2c (refer to Supplementary Fig. 6 for the MD snapshots for the remaining solvents). From the snapshots, we can observe the prevalence of water clusters in the presence of ACN and PC media, whereas there is a preferential formation of water–solvent bonds dispersed in the DMSO matrix.

The differences in water solvation can also be understood based on solvent– H_2O energetics. Due to the directional behaviour of the HB interactions, we expect an increase in HB angle as HB acceptors and donors approach a colinear conformation (θ = 180°). Figure 2d shows an increase in the OH–solvent angle accompanied by a decrease

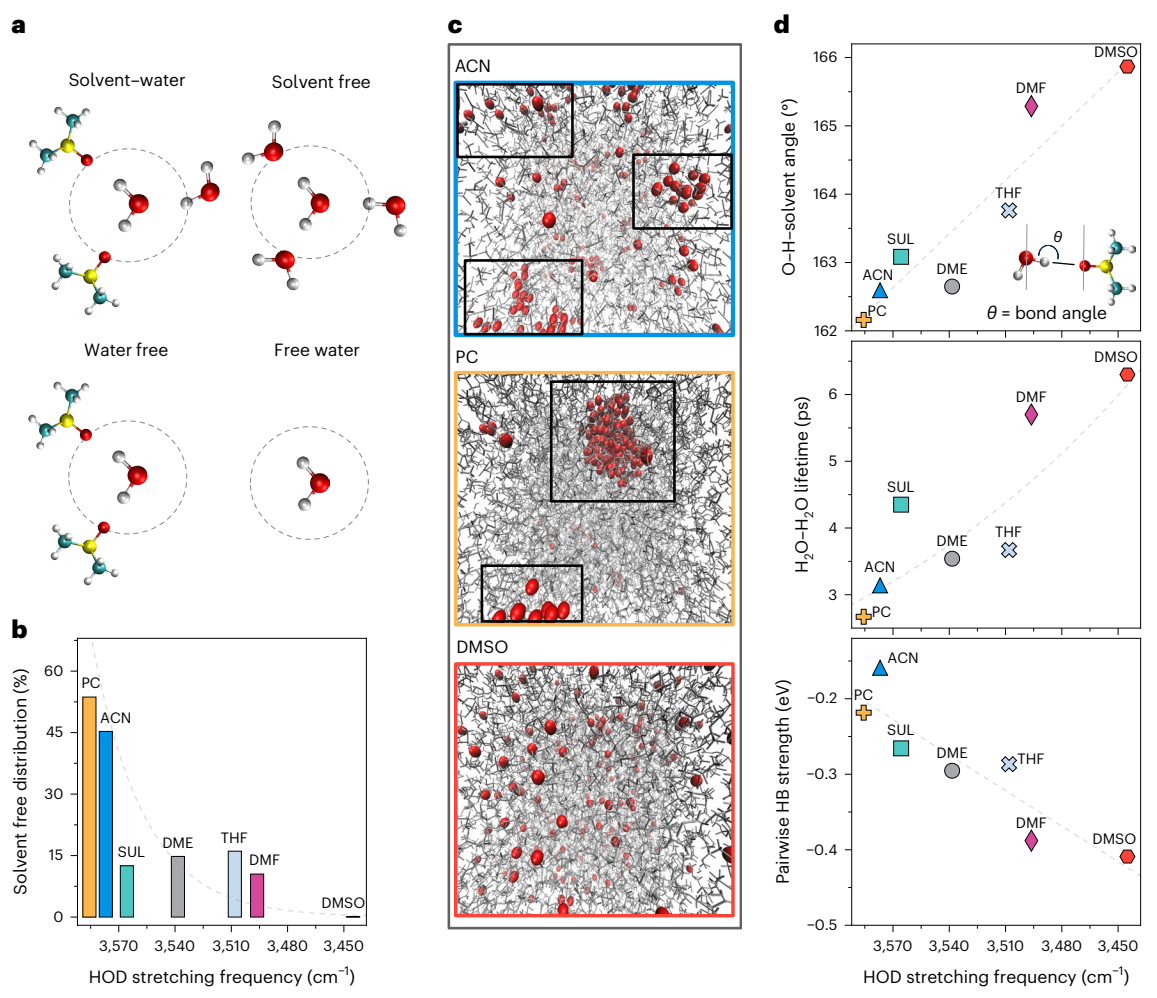


Fig. 2 | Water clustering and dynamics. a, Illustration of different water solvation structures. b, Correlation between water solvent-free distribution calculated from MD simulations and experimental water HOD stretching frequency for 1 M water in different solvents. c, Molecular dynamics snapshots of systems containing 1 M water in selected solvents. The highlighted area indicates

the presence of water clusters. \mathbf{d} , Correlations between water OH–solvent angle and the water–water lifetime calculated from MD simulations, the pairwise HB strength from DFT calculations and the HOD stretching frequency extracted from Fig. 1e for 1 M water in different solvents. Dashed lines are to guide the eyes.

in the O–H stretching frequency. Again, we observe stronger solvent– $\rm H_2O$ interactions for DMSO and DMF compared with PC and ACN. The differences in HB energetics may also play a role in water HB dynamics. Figure 2d shows that the water–water lifetime scales with HOD stretching frequency, indicating a cooperative effect (that is, when the HB of two molecules are modified by the presence of a third) of the solvent on the water–water dynamics. Supplementary Fig. 7 also shows a slight increase in water–solvent HB lifetime as HOD redshifts, with an exception for DMSO, which presents a much longer HB lifetime than the other solvents.

To gain a more quantitative understanding of the solvent–water HB strength, we performed DFT calculations to quantify their pairwise HB strength. This pairwise interaction can serve as an average local probe, acting as a reliable proxy for the entire HB network strength in a solvent–water system (see Supplementary Note 2 and Supplementary Table 3 for further details on DFT calculations). Trends in Fig. 2d reveal that a solvent with higher donor ability such as DMSO and DMF forms stronger interactions with water, while also slowing down its HB dynamics. By contrast, ACN and PC can form weaker water HB networks with faster dynamics. Our findings are in accordance with previous studies that have shown that either an increase in solvent concentration⁴⁷ or a decrease in temperature⁴⁸ can promote a blue shift in O–H stretching frequency and a decrease in HB lifetime. Here we demonstrate that

the water solvation and dynamics can also be tuned through solvent selection for different water in solvent mixtures.

Solvent effect on the HER

The role of different solvent— H_2O interactions in modulating HER activity was probed. We chose tetrabutylammonium (TBA+) perchlorate as a supporting electrolyte to minimize any competing effects from water—cation and solvent—cation interactions. It has been shown that the butyl chain in TBA+ hinders short-range interactions with either water or organic solvents, unlike what is observed for harder alkali cations such as Li+ (refs. 22,25,49). However, we do not rule out the possibility of TBA+ making the electrode surface more hydrophobic, as proposed by others^{3,22}. For a systematic comparison of the HER activity, we kept the supporting electrolyte and its water mole ratio (0.1 M/1 M) constants across all solvents studied here. We do not observe any substantial change in the water 1 H NMR spectra when the TBA salt is present (Supplementary Fig. 8). The applied potential was referenced to the internal redox standard decamethylferrocene (Me₁₀Fc) to correct solvent effects on the quasi-reference electrode potential.

The voltammograms in Fig. 3a for a flat, polycrystalline rotating disk Au electrode at 1,600 r.p.m. show that different aprotic solvents present significant differences in HER activity. Those differences can't be assigned to either solution conductivity or water mole fraction

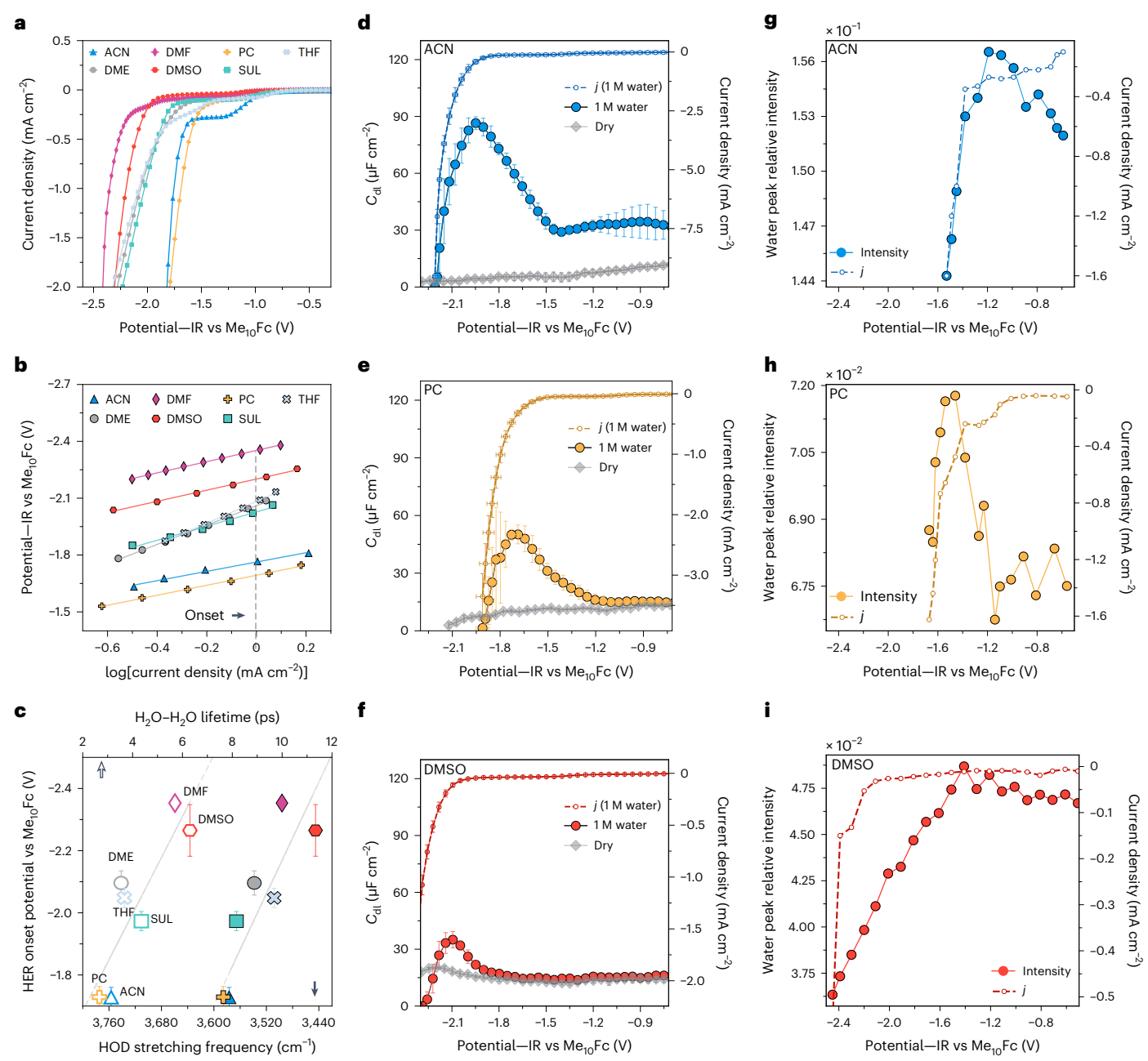


Fig. 3 | **Influence of water solvation on HER. a**, Linear sweep voltammograms at 5 mV s⁻¹ over a rotating gold disk electrode at 1,600 r.p.m. for different solvents containing 1 M water and 0.1 M TBAClO₄. **b**, Tafel plots from the data collected in **a. c**, Onset potentials collected from **b** at 1 mA cm⁻² versus HOD stretching frequencies collected in Fig. 1e (solid symbols) and the H₂O-H₂O lifetime (hollow symbols). Grey lines are a guide to the eyes. **d-f**, Double-layer capacitance values and current density values averaged over 1 min during electrochemical impedance spectroscopy experiments for solutions containing 0.1 M TBAClO₄

in ACN (**d**), PC (**e**) and DMSO (**f**) over a rotating RDE gold disk electrode at 1,600 r.p.m. under dry conditions (water content < 50 ppm) and in the presence of 1 M water. *j* corresponds to the current density. **g**–**i**, Relative intensity values between the water and solvent/TBA peaks calculated from the in situ SERS spectra, and current density values averaged over 2 min of chronoamperometric experiments at different potentials for solutions containing 0.1 M TBAClO₄ and 3 M water in ACN (**g**), PC (**h**) and DMSO (**i**). Data are presented as mean values (**c**–**f**) and error bars represent \pm s.d. from three experiments.

(Supplementary Table 4). Experiments under dry conditions confirm that the cathodic current originates from HER and not from electrolyte decomposition (Supplementary Fig. 9). The cathodic current observed for ACN around -1.0 V has been reported by others^{22,23} and could be attributed to either cyanide formation or residual oxygen reduction, which becomes diffusion-limited before the distinct cathodic feature for HER takes place.

For a quantitative assessment of HER activity, we arbitrarily determined the HER onset potential as the point at which the current density reaches 1 mA cm $^{-2}$ at 1,600 r.p.m. This value lies within the linear Tafel

regime for all solvents, as shown in Fig. 3b. Without a strict definition for the HER onset potential 50,51 , we opted for its determination within this regime to minimize the effect of mass transport limitations on current density, as transport-related physical properties (such as viscosity) greatly vary across solvents (see Supplementary Table 1). As shown in Fig. 3c, the onset potential for the HER increases as O–H stretching frequency decreases, indicating that the strength of the water HB network plays an important role in its electrochemical activity. Solvents that form a strong water HB, such as DMF and DMSO, can suppress HER to potentials as negative as -2.4 V versus Me_{10} Fc. By contrast, solvents with

weaker water–solvent interactions (for example, ACN and PC) exhibit higher HER activity with onset values of around –1.7 V. For solvents with moderate HB strengths (SUL, DME and THF), the HER onset lies in intermediate values. A similar effect is observed between HER and water–water dynamics, where an increased water–water HB lifetime leads to higher onset potentials for HER.

The correlation between water electrochemical activity and its HB network strength is consistent with proposed mechanisms for the HER. Different studies using in situ vibrational^{7,8} spectroscopy and X-ray absorption spectroscopy⁵ have shown that during water reduction, water needs to first undergo interfacial reorientation accompanied by HB breakdown. We therefore hypothesize that one could increase water availability and mobility near the electrode surface by changing the enthalpic penalty associated with HB breakdown, and consequently increase HER activity. We can probe the water availability at the electrode surface by comparing the double-layer capacitance values ($C_{\rm dl}$) before and after the addition of water. As water molecules have a higher dielectric constant than all of the aprotic solvents studied here (Supplementary Table 1), and undergo accumulation and reorientation before the HER, we may expect an increase in C_{dl} as a function of water availability at the electrode interface. Further considerations, circuit model, and fitting parameters used for the $C_{\rm dl}$ analysis can be found in Supplementary Note 3 and Supplementary Figs. 10 and 11.

Figure 3d-f show the $C_{\rm dl}$ results at different potentials for some selected solvents. We chose ACN and DMSO due to the stark differences in water solvation structure and HER activity; PC was added because it presented similar water solvation behaviour to ACN, but physicochemical properties unlike ACN when compared with DMSO, such as dipole moment, density, molar mass and viscosity (Supplementary Table 1). All three solvents also present good wettability over the gold surface (Supplementary Fig. 12). Figure 3d-f shows a substantial increase in $C_{\rm dl}$ after the addition of water for ACN and PC, but not for DMSO. As we hypothesized, solvents with higher water reactivity presented a significant increase in capacitance before its onset potential, indicating that water molecules might be accumulating and reorienting at the electrode surface before reduction. In contrast, the stronger water-solvent interactions in DMSO slow down not only water-water dynamics in the bulk but also its availability and reorientation at the electrode-electrolyte interface.

The water availability under electrochemical conditions was further investigated by in situ surface-enhanced Raman spectroscopy (SERS), as shown in Fig. 3g-i (see Supplementary Note 4 and Supplementary Fig. 13 for further details). A significant increase in water peak intensity relative to solvent/TBA peaks was observed for ACN and PC before a subsequent sharp decline in current density. These findings suggest a preferential accumulation of water at the electrode surface preceding the HER. At more negative potentials, the pronounced decrease in water intensity can be attributed to its consumption. Conversely, in DMSO, the water relative intensity decreases before a notable decline in cathodic current, indicating the accumulation of solvent and/or TBA⁺ molecules at a more negatively polarized electrode. This distinction in solvent behaviour may contribute to the observed larger overpotentials for HER in DMSO. It is worth noting that we used a water concentration of 3 M for the in situ SERS experiments to overcome the lower sensitivity of Raman spectroscopy towards water molecules. Nevertheless, the trends observed in the in situ SERS analysis are in agreement with our electrochemical and C_{dl} results. Replicates for independent in situ SERS experiments can be found in Supplementary Fig. 14.

Enhancing CO₂ electrochemical reduction selectivity

We explore the ability of different solvent—water interactions in tuning the selectivity of the CO_2R . Figure 4a-c shows voltammograms for CO_2 -saturated solutions of selected solvents in the presence and absence of water and CO_2 . When only water is present, the cathodic

features are assigned to the HER, which shifts to lower overpotentials as the water content increases. Under dry conditions (grey lines), the cathodic current can be assigned to the $\mathrm{CO}_2\mathrm{R}$. Interestingly, $\mathrm{CO}_2\mathrm{R}$ occured at lower overpotentials for DMSO than for ACN and PC. This observation allows us to rule out the hypothesis that differences in the HER onset potential originate from solvent blockage of the electrode active sites. If these blockages were occurring in DMSO, we would also anticipate a pronounced increase in the $\mathrm{CO}_2\mathrm{R}$ overpotential.

When both CO_2 and water are present in the sample, we observed a distinct cathodic feature at more positive potentials than either CO_2R or HER for all three solvents. This new feature has been associated with the promoting effect of water on CO_2R , where water can act as a proton donor and stabilize key CO_2R intermediates (for example, *CO and *COOH), resulting in lower overpotentials 21,52. This promoting effect was more substantial for PC and ACN than for DMSO, decreasing the overall overpotentials for CO_2R by 930, 720 and 140 mV, respectively, at 1 mA cm⁻² in the presence of 1 M water. Those results agree with our $C_{\rm cl}$ values and in situ SERS experiments, which also revealed a greater availability of water at the electrode interface for ACN and PC.

We further investigated the competition between the CO₂R and HER in different solvents using an H-cell set-up. The gold electrode is especially suitable for these studies as it predominantly yields CO and H₂. The product distribution analysis at different potentials in the selected solvents is shown in Fig. 4d-f. For solutions containing 1 M water, we don't observe any H₂ across different potentials for all three solvents, with nearly 100% FE values towards CO; however, the H₂ FE increases with water content for solvents that form weaker HB networks with water. For PC, we observe H₂ FE values of around 50% and 30% at 2 M and 3 M, respectively. For ACN, we observe the significant production of H_2 for potentials as negative as -1.8 V, with FEs for H_2 of around 5% and 20% for 2 M and 3 M water respectively. In contrast, only trace amounts of H₂ were observed for DMSO, leading to FE values towards CO of 100% for water concentrations as high as 3 M. By tuning the water HB network environment, one can ensure the total selectivity of CO₂ to CO, while still benefiting from the decrease of CO₂R overpotential promoted by the presence of water.

Although the water confinement within a strong HB network may lead to a high CO selectivity, it does not explain the significant differences in H₂ FE between PC and ACN at higher water contents. A possible reason why CO₂R might be outperforming HER at lower overpotentials in ACN but not PC could be related to differences in CO₂ solubility across these solvents. The CO₂ solubility at room temperature and ambient pressure lies around 170 mM (ref. 53) and 130 mM (ref. 54) for PC and DMSO, respectively. In contrast, it reaches values greater than 300 mM for ACN55. A higher CO2 solubility coupled with lower viscosity (Supplementary Table 1) may result in a higher CO₂ mass transfer in ACN, which others have shown favours CO₂R over the HER⁵⁶⁻⁵⁸. It is worth noting that ACN solutions also present an ionic conductivity of 8.1 mS cm⁻¹—around four-times greater than those observed for PC (1.9 mS cm⁻¹) and DMSO (2.3 mS cm⁻¹), as shown in Supplementary Table 4. The high CO₂ mass transfer and solution conductivity in ACN may explain the superior CO partial current densities, which are roughly five-times higher than those in PC and DMSO for 1 M water (Supplementary Fig. 15). Therefore, CO₂R selectivity may not only be achieved by the solvent's ability to suppress the HER (that is, by using DMSO) but also by enhancing CO₂ mass transfer and solution ionic conductivity.

Next we investigated the water kinetic isotopic effect (KIE) to elucidate whether the differences in water HB strength and arrangements could play a role in the reaction pathways of both the HER and $\mathrm{CO}_2\mathrm{R}$. As CO is the only product observed on CO_2 -saturated solutions containing either 1 M water or 1 M $\mathrm{D}_2\mathrm{O}$ (Supplementary Fig. 16), KIE values can be obtained directly from the step sweep voltammograms shown in Fig. 5. All argon-saturated solvents exhibited KIE values of 2.2 to 3.4 for the HER. This entails that breaking the O-H bond in water and/or forming the H-H bond are involved in the rate-determining

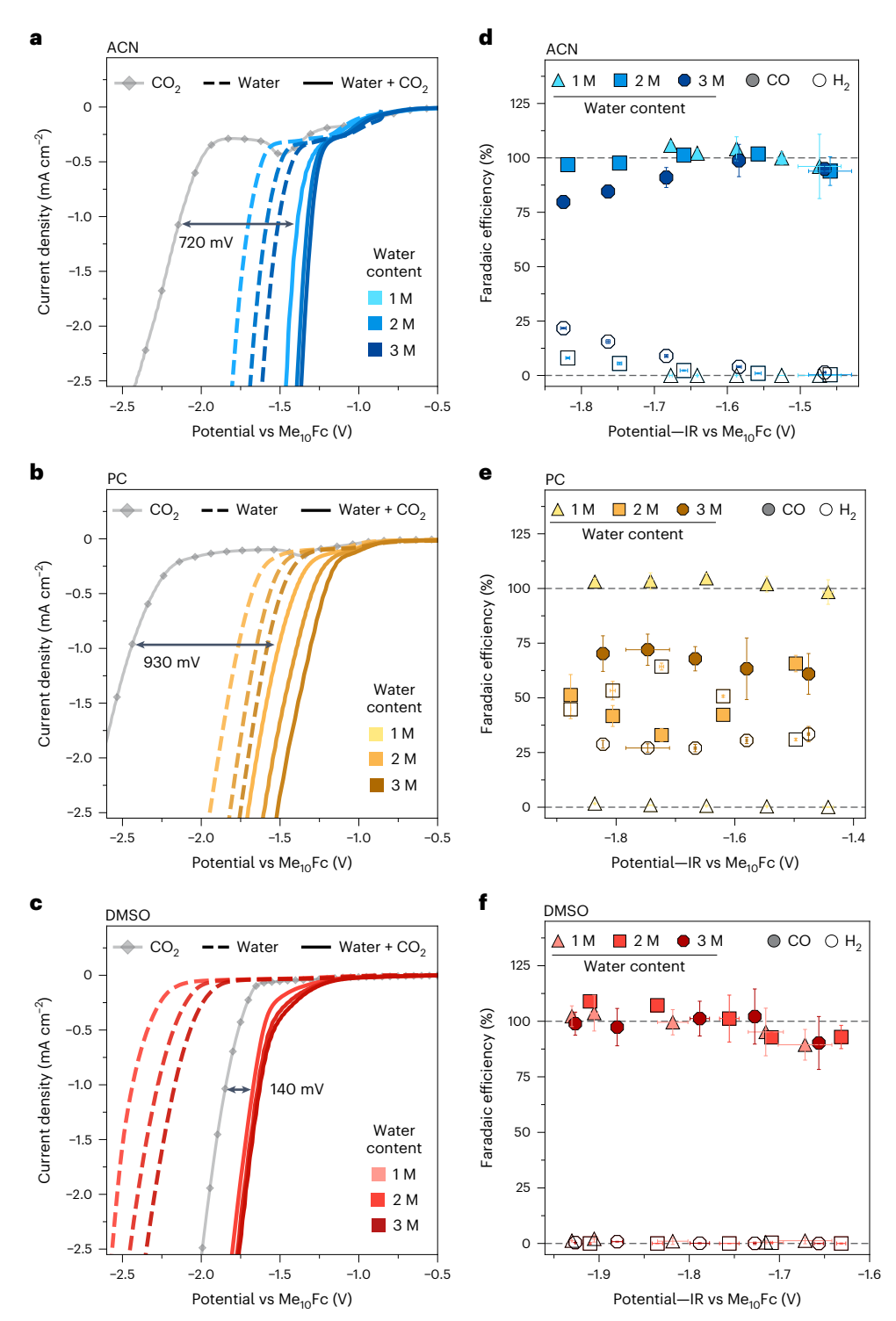


Fig. 4 | **Influence of water addition on CO₂R. a**-c, Linear sweep voltammograms at 5 mV s⁻¹ over a gold disk electrode at 1,600 r.p.m. for CO₂-saturated solutions containing 0.1 M TBAClO₄ in the presence and absence of water in ACN (a), PC (b) and DMSO (c). The grey lines are for dry solutions (water content < 50 ppm) saturated with CO₂. The dashed lines are for solutions containing water at different concentrations (1 M, 2 M and 3 M) in an argon atmosphere, whereas the solid lines are the respective solutions saturated with CO₂. The black arrows

indicate the difference in the potential between the dry CO_2 saturated solution, and the corresponding solution containing 1 M water. \mathbf{d} – \mathbf{f} , Product distribution analysis using an H-cell set-up for solutions in \mathbf{a} (\mathbf{d}), \mathbf{b} (\mathbf{e}) and \mathbf{c} (\mathbf{f}) saturated with CO_2 and containing 1 M (triangles), 2 M (squares) and 3 M water (octagon). Solid and hollow icons are used for the FE of CO and H_2 , respectively. Data are presented as mean values and error bars represent \pm s.d. from three experiments.

step⁵⁹. Conversely, for CO_2R , all solvents consistently exhibited KIE values of 1 across various potentials (Fig. 5d-f), indicating that the hydrogenation of CO_2 does not contribute to the rate-determining step. To further investigate potential reaction pathways for CO_2R , we

conducted DFT calculations to evaluate the CO_2R free-energy profiles in the presence and absence of water (refer to Supplementary Note 5, Supplementary Fig. 17, and Supplementary Tables 5, 6 and 7 for more details). Our findings indicate that water facilitates a facile reaction

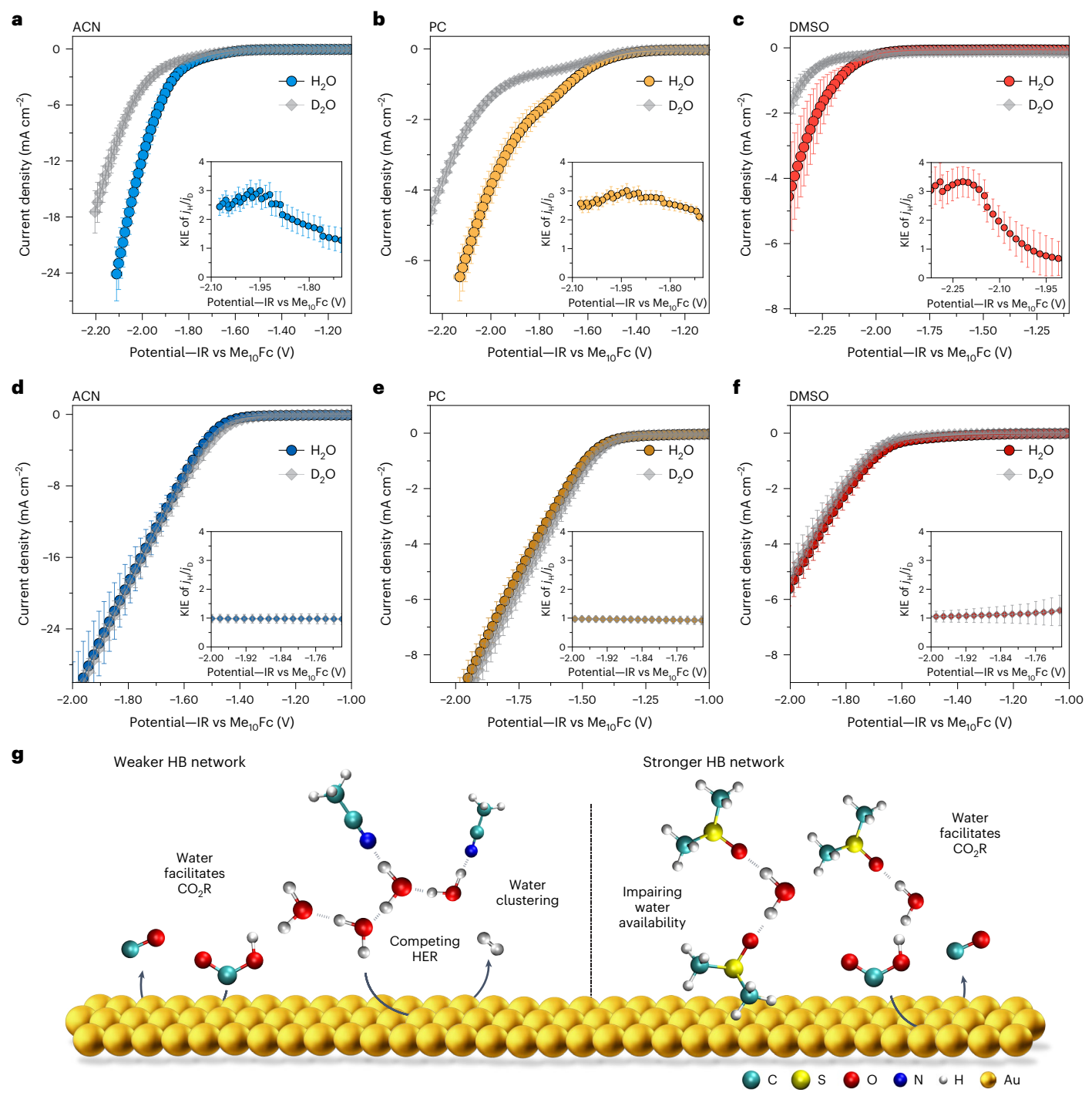


Fig. 5 | **Effect of water solvation on kinetics. a**–**f**, Step sweep voltammograms (50 mV steps held for 5 s each) of argon-saturated solutions of ACN (**a**), PC (**b**) and DMSO (**c**), and CO₂-saturated solutions of ACN (**d**), PC (**e**) and DMSO (**f**). All solutions contain 0.1 M TBAClO₄, and 1 M H₂O or 1 M D₂O. Electrochemical experiments were performed over a gold rotating disk electrode at 1,600 r.p.m. under a constant purge of either argon or CO₂. Kinetic isotope effect values were

calculated by dividing the current densities (j_H/j_D) for H_2/D_2 (**a-c**) or CO (**d-f**) for the same applied potential. Data are presented as mean values and error bars represent \pm s.d. from three experiments. **g**, Illustration of the effect of solventwater interactions on the water availability, HER activity and CO_2R selectivity at the gold electrode surface.

pathway for CO_2 reduction compared with dry conditions. The effect of the solvent on the water HB network and HER and CO_2 R selectivity is illustrated in Fig. 5g.

Enhancing CO₂R selectivity in a mildly acidic medium

Another side reaction that compromises CO_2R deployment is the formation of carbonate species 26 . Carbonate and bicarbonate are formed

during the reaction of CO_2 with OH^- in situ generated from either CO_2R or the HER (equations (1–3)).

$$CO_2 + H_2O + 2e^- \rightarrow CO + 2OH^-$$
 (1)

$$H_2O + e^- \rightarrow \frac{1}{2}H_2 + OH^-$$
 (2)

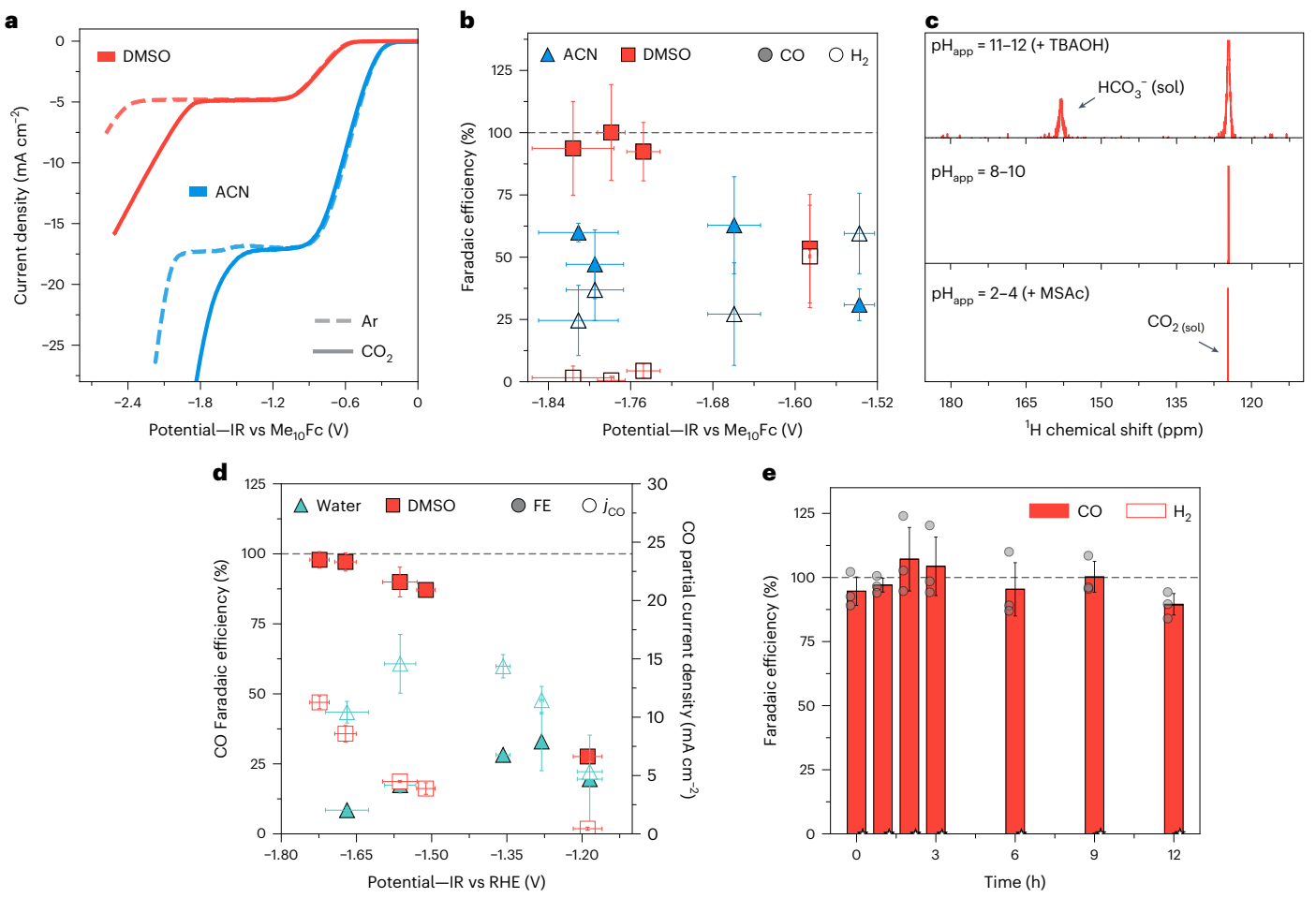


Fig. 6 | **Electrochemistry under acidic conditions. a**, Linear sweep voltammograms at 5 mV s⁻¹ over a gold disk electrode at 1,600 r.p.m. for solutions containing 0.1 M TBAClO₄, 1 M water and 10 mM MSAc in the presence and absence of CO_2 in ACN and DMSO. **b**, Product distribution analysis for solutions in **a** using a gold electrode. **c**, ^{13}C NMR of DMSO solutions containing dissolved $^{13}CO_2$. The initial solution (middle spectrum) contains 0.1 M TBAClO₄ and 1 M water, exhibiting a pH_{app} of around 8–10. The solution represented by the spectrum at the top also contains 5 mM TBAOH (pH_{app} = 11–12), whereas the one

on the bottom also contains 10 mM MSAc (pH_{app} = 2–4). **d**, Product distribution analysis and CO partial current density values ($j_{\rm CO}$) for the DMSO solution in **a** (red), and an aqueous electrolyte containing 100 mM KHCO₃ and 100 mM H₃PO₄ (turquoise), using a zinc electrode. **e**, Product distribution analysis for DMSO solution in **b** using a zinc electrode at –10 mA cm⁻² over 12 h electrolysis. Data are presented as mean values (Fig. 6b,d,e) and error bars represent \pm s.d. from three experiments.

$$CO_2 + 2OH^- = CO_3^{2-} + H_2O$$
 (3)

Thus, conducting CO_2R under an acidic environment is of special interest because H^+ can react with carbonate species, restoring CO_2 . However, the reaction selectivity in an acidic medium is commonly plagued by the HER from proton reduction, which happens at more positive potentials than water. Different strategies in aqueous conditions have been explored 27,60 , but none can effectively reach 100% FE values because water reduction still happens at a similar potential as CO_2R .

To further extend the effect of solvent— H_2O interactions on CO_2R selectivity, we conducted a product distribution analysis of our two best-performing solvents, DMSO and ACN, in a mildly acidic medium. In a past work^{24,25}, our group showed that carbonate formation can be mitigated during CO_2R in DMSO after the addition of methanosulfonic acid (MSAc). Here we tested the same hypothesis, but at a lower acid concentration (10 mM MSAc), and in the presence of 1 M water and 0.1 M TBA salt. In the absence of CO_2 , the first cathodic feature can be assigned to proton reduction, which remains mass transport limited until water reduction starts to dominate at more negative potentials (Fig. 6a). Similarly to what we had observed for the HER from water, ACN

presents a higher activity for proton reduction than DMSO, with limiting current density values of around 17 mA cm $^{-2}$ and 5 mA cm $^{-2}$, respectively. When CO_2 is added to the system, we observe a new cathodic feature assigned to CO_2R , happening at potentials between the water and proton reduction for both solvents. Product distribution analysis for acidic ACN and DMSO (Fig. 6b) shows significant HER activity for both solvents at -1.6 V, when the CO_2R starts to take place. However, the FE values for CO in DMSO reach values around 100% for potentials more negative than -1.8 V. In contrast, we still observe FE values for H_2 of greater than 20% in ACN between -1.7 and -1.8 V. Those findings revealed that the nature of the solvent also plays a significant role in CO_2 selectivity under acidic conditions.

Later, we used 13 C NMR to probe the carbonate speciation under different pH conditions in DMSO. We used MSAc and TBA hydroxide to bring the apparent pH (pH_{app}) to acidic and basic values, respectively. We define neutral conditions as the solution's pH_{app} when neither acid nor base was added (pH_{app} = 8–10). As shown in Fig. 6c, we can only observe a single peak at 125 ppm, which is assigned to CO₂ under acidic (pH_{app} = 2–4) and neutral conditions; however, under basic pHs (pH_{app} = 11–12), a new peak assigned to HCO₃⁻ can be observed at 158 ppm. During the H-cell experiments in DMSO, using a gold electrode under neutral conditions, the pH increased from 8.8 ± 0.6 to

 11.2 ± 0.5 , indicating that CO_2 has been depleted to some extent through bicarbonate formation. However, during H-cell experiments under acidic conditions, the pH remained steady at 2.9 ± 0.2 after 6 h of the experimental run (Supplementary Table 8). At this pH, we may then expect a theoretical carbon efficiency (that is, the number of CO_2 molecules used towards CO_2R products divided by total number of CO_2 fed into the system) of 100%, as no carbonate species will be present in the bulk electrolyte.

As suppression of proton reduction is in principle an electrolyte effect, we hypothesized that similar results could be accomplished with different catalysts. We therefore conducted a product distribution analysis in acidic DMSO using an earth-abundant zinc electrode instead of gold. Flat polycrystalline zinc electrodes yield mostly CO in a non-aqueous medium, but it is also subjected to carbonate losses¹⁹. Furthermore, its CO selectivity does not exceed 50% when in an aqueous environment⁶¹⁻⁶³. Figure 6d shows the product distribution for a flat zinc polycrystalline disk in DMSO containing 1 M water and 10 mM MSAc. For a direct comparison with CO₂R performance in an aqueous medium, the cell potential was benchmarked against the reversible hydrogen electrode (RHE). There are many challenges involving the determination of the proton activity in a non-aqueous medium due to multiple solution non-idealities⁶⁴. However, we can estimate the H₂/H⁺ equilibrium potential in DMSO using a leakless hydrogen electrode (see Supplementary Note 6). The CO₂R product distribution analysis for an aqueous electrolyte composed of KHCO3 and H3PO4 is also shown in Fig. 6d. Both aqueous and non-aqueous electrolytes presented a pH and p H_{app} of around 4 (Supplementary Table 8). For an aqueous medium, we observed a peak CO FE of approximately 42% at -1.3 V versus RHE. However, at higher overpotentials, the CO FE sharply decreases to below 5%, even though its partial current density increases to values between 14.5 ± 3.5 mA cm⁻² at -1.56 V versus RHE. This decline in CO selectivity can be attributed to the increase in the competing HER (Supplementary Fig. 15). In contrast, the utilization of a non-aqueous DMSO electrolyte yields CO FE of 98 ± 3% at -1.7 V versus RHE. This performance is accompanied by CO partial current densities of 11.5 \pm 1 mA cm⁻², within a similar range observed in aqueous media at similar potentials.

Finally, we probed the stability of the acidic DMSO electrolyte over 12 h electrolysis. The FE values for a galvanostatic experiment at $10~\text{mA}~\text{cm}^{-2}$ over a zinc electrode are shown in Fig. 6e. Although discernible DMSO and TBA decomposition products are detectable at the 12 h mark, especially in the anolyte (Supplementary Fig. 18), we observe CO FE values around 100% for up to 9 h of experiments. The electrolyte therefore seems to be stable over a long experimental period.

Conclusion

The framework developed in this work revealed how water solvation behaviour in aprotic solvents can tune HER activity and CO₂R selectivity. Our spectroscopic studies, MD simulations and DFT calculations showed that solvents with a high donor number can form strong HB networks with water while increasing the water-water HB lifetimes. We then demonstrated how the solvent's impact on the water HB strength and dynamics could be used as descriptors for HER activity by demonstrating a quasi-linear correlation with the HER onset potential over a gold electrode. The increase in HER activity also aligns with an increase in water availability near the electrode surface. When CO₂ is added to the solution, we observed that CO₂R selectivity can be dictated by both the solvent ability to suppress the HER and enhance CO₂ mass transfer. We also show that CO₂R selectivity can also be tuned in an acidic non-aqueous environment by using a solvent with a high donor number to suppress proton reduction. These findings enabled the use of a non-precious metal zinc catalyst with nearly 100% FE towards CO with no carbonate losses up to 9 h of electrolysis. These findings provide descriptors and fundamental insights to guide electrolyte selection and control water reactivity in a wide range of desired electrochemical transformations such as the HER, CO_2R , COR and nitrogen reduction, among others.

Methods

General procedures

Tetrabutylammonium perchlorate (Alfa Aesar, 99%) was dried under vacuum at 100 °C for 24 h and stored inside an argon-filled glovebox (Vigor, $O_2 < 1$ ppm, $H_2O < 1$ ppm). All other reagents were used as received, unless stated otherwise. Acetonitrile (anhydrous, 99.8%), 1,2-dimethoxyethane (anhydrous, 99.5%, inhibitor-free), dimethylformamide (anhydrous, 99.8%), DMSO (anhydrous, 99.9%), propylene carbonate (anhydrous, 99.7%), sulfolane (99%) and tetrahydrofuran (anhydrous, 99.9%, inhibitor-free) were all purchased from Sigma-Aldrich and moved to an argon-filled glovebox before opening. After the dissolution of salts, all electrolytes exhibited a water content of lower than 50 ppm, except for the sulfolane solutions, which exhibited concentrations of around 450 ppm (Supplementary Table 9). Tetrabutylammonium hydroxide 30-hydrate (99%), MSAc (99%), potassium bicarbonate (99.95% trace metals), phosphoric acid solution (80 wt% in H₂O) and tetramethylsilane (99%) were also purchased from Sigma-Aldrich. All glassware used was cleaned by first rinsing them with soap and subsequently three times with ethanol (Fisher, 70%), isopropanol (StatLab, 99%) and Mili-Q water (resistivity 18.2 M Ω cm at 25 °C). They were then rested in a fresh acid bath containing 3% (v/v) HNO₃ solution (Fisher Chemical, TraceMetal Grade) for 24 h, rinsed again three times with Mili-Q water and dried at 80 °C for 2 h before use. Molecular sieves (Sigma, 3 Å) were activated by vacuum drying at 210 °C for 24 h before use.

Infrared and Raman scattering spectroscopy analysis

Infrared spectra were collected using a Shimadzu IRTracer-100 Fourier-transform infrared spectrophotometer with a GladiATR (diamond prism) featuring a single-bounce-attenuated total reflection (ATR) attachment. A spectral resolution of 1 cm⁻¹ was used for the HOD experiments, with an average of 40 scans per sample. A PTFE cap was used on top of the diamond prism to prevent solution evaporation. Raman spectra were collected using a HORIBA LabRAM HR Evolution Confocal Raman Microscope equipped with a 532 nm laser as a light source and a cuvette adaptor. The samples were placed inside a quartz cuvette (Starna, Infrasil Quartz) and sealed with a PTFE cap. Sample signals were accumulated over 3 s and averaged over 40 scans. Peak deconvolution and fitting were performed using the CasaXPS software⁶⁰, using a linear background correction and Savitzky-Golay filter (11th-degree polynomial) for smoothing of the data. Due to the complexity of predicting all possible HB configurations for water/solvent mixtures, we deconvolute those peaks, leaving free their number, position and full-width at half-maximum; however, we centred the free water peak at $3,650 \pm 30 \text{ cm}^{-1}$, as it is distinct from all of the other possible HB configurations.

NMR spectroscopy characterization

All samples were prepared inside an argon-filled glovebox. A co-axial capillary set-up was used, where the electrolyte samples were placed inside of a 5 mm NMR tube, whereas the deuterated solvent (chloroform-D, Cambridge Isotope Laboratories, 99.8%) was placed inside the capillary tube (New Era Enterprises) and sealed with a PTFE cap; 10 mM tetramethylsilane was added to all samples (NMR tube) and used as an internal reference (0 ppm). All ¹H NMR spectra were collected using a Bruker Ascend 9.4 T/400 MHz.

Classical molecular dynamics and DFT calculations

The classical MD simulations were conducted using the large-scale atomic/molecular massively parallel simulator ⁶⁵ simulation package (September 2021) ⁶⁶. The simulation boxes for MD calculations are prepared such that they reproduce the experimental densities of

the corresponding pure solvents, and the water molecules are added subsequently to yield a concentration of 1 M. Density functional theory calculations were conducted using Gaussian (v.16 Revision A.03)⁶⁷. Refer to Supplementary Notes 1, 2 and 5 for further details on MD simulations, force-fields applied, box size, number of molecules and DFT calculations.

Electrochemical measurements

All voltammetric experiments were acquired inside an argon-filled glovebox using a Biologic VSP potentiostat. A flat rotating gold disk (Pine Research, PTFE tube, OD 5.0 mm) was used as the working electrode, whereas a folded gold wire was used as the counter electrode (Thermo Scientific, 99,999% metals basis, 20 cm length, OD 0.25 mm). A Pine Research MSR rotator was used. An Ag/AgCl leakless electrode (eDAQ, PEEK tube) was used as a pseudo reference electrode, which was calibrated after each electrochemical measurement by the addition of 2 mM Me₁₀Fc (Sigma, 99%) to the electrolyte sample. The experiments were conducted inside a 25 ml three-neck round-bottom flask. Either argon or CO₂ was continuously purged into the flask during the experiments. Residual water was removed from the gases by a custom-made filter composed of a PTFE tube filled with activated molecular sieves. After each experiment, the uncompensated resistance was acquired at three different potentials (-0.5, -1.5 and -2.5 V versus Ag/AgCl) at the high-frequency regime (10 kHz) of the electrochemical impedance spectra. No significant changes were observed for uncompensated resistance values across these potentials for all samples. All potentials were reported after 100% manual after-the-scan Ohmic drop (IR) compensation using the average uncompensated resistance value for each electrolyte.

Capacitance double-layer measurements

We investigated C_{dl} using electrochemical impedance spectroscopy, by fitting the experimental results with a circuit composed of a constant phase element and a resistor in series. The circuit model used and the fitting parameters can be found in Supplementary Figs. 10 and 11, respectively. The C_{dl} values were acquired in a 25 ml three-neck round-bottom flask using step-potential electrochemical impedance spectroscopy inside an argon-filled glovebox connected to a Biologic VSP potentiostat; 50 mV steps were used, with a 5 s waiting time between each potential. To keep the experiment within a reasonable timeframe and prevent further electrode restructuring or dissolution. the scan frequency ranged from 1 KHz to 1 Hz—with ten points per decade-and was averaged over three measurements. A sinus amplitude of $35 \,\mathrm{mV} \,(\mathrm{V}_{\mathrm{rms}})$ was applied. A rotating gold disk electrode and gold wire were used as working and counter electrodes, respectively. A leakless Ag/Ag⁺ electrode was used as a reference electrode. Electrode calibration against Me₁₀Fc and IR compensation were done as previously described. The fitting for the Nyquist plot simulations was made using the Python package impedance.py 1.4 (ref. 68).

In situ SERS analysis

Refer to Supplementary Note 4 for further details on electrode preparation, cell design, and data acquisition and processing.

Product distribution analysis

The product distribution was investigated using a glass H-cell, in which a graphite rod (Fisher, OD 6.15 mm, 99.995% metal basis) was used as the counter electrode, a leakless Ag/AgCl as the reference electrode, and a gold (eDAQ, OD 3 mm) or zinc (Fisher, 99.994% trace metals basis, OD 3.18 mm) disk was used as the working electrode. Both catholyte and anolyte chambers were filled with the same solutions, which were separated by a Nafion-N117 (Alfa Aesar) proton exchange membrane. Procedures for the elimination of acid residues from the membrane are described in Supplementary Note 7. A stir bar at 750 r.p.m. was kept at the catholyte chamber, while a constant

 $\rm CO_2$ (Air Gas, 99.9995%) flow of 10 sccm was fed into the solution. The $\rm CO_2$ inlet tubing was placed in a manner such that the gas bubbles did not hit the cathode surface. Products in the gas phase were analysed using a Shimadzu GC-2014 in-line gas chromatograph with both flame ionization and thermal conductive detectors. Products in the liquid phase were analysed using 1H NMR in a Bruker Ascend 9.4 T/400 MHz instrument. The reference electrode calibration against Me $_{10}$ Fc was performed before each H-cell experiment using a three-electrode Beaker cell with the gold disk as the working electrode and platinum disk as the counter electrode. Ohmic drop compensation was performed as previously described.

General procedures for electrode cleaning

Gold and platinum electrodes were gently polished with alumina slurry (eDAQ). The electrodes were then rinsed with ethanol, isopropanol and Mili-Q water. High-pressure N_2 (Airgas, ultra-high purity grade) was used to remove any excess alumina slurry from the electrode surface. The electrodes were stored in fresh $0.5\,\mathrm{M}$ sulfuric acid solution for at least 24 h. Before each electrochemical measurement, the electrodes were rested for 1 h in 3% (v/v) HNO $_3$ TraceMetal-grade solution and rinsed again with Mili-Q water. Graphite rods were used as received. Zinc electrodes were first rinsed with ethanol, isopropanol and Mili-Q water, and then intensely polished with alumina slurry to remove any superficial oxide layer before each experiment. The excess alumina slurry was removed by rinsing the electrode with Mili-Q water and using a high-pressure N_2 blow at the electrode surface.

¹³CO₂ speciation studies

 13 C-labelled CO₂ (MilliporeSigma, 99 at% 13 C and 99.93 at% 16 O) was purged for 5 min at 5 sccm into 2 ml of sample; CO₂ and carbonate were identified using 13 C NMR in a Bruker Ascend 9.4 T/400 MHz.

pH measurements

The pH measurements were taken with a Mettler–Toledo SevenCompact pH meter with a pH probe Sensor InLab Smart Pro-ISM. The pH probe uses Xerolyt polymer as a reference electrolyte and has an open junction to eliminate the possibility of clogging and contamination with the non-aqueous electrolytes used. The pH measurements taken in a non-aqueous medium are reported as pH $_{\rm app}$.

Data availability

Molecular dynamics inputs, initial and final configurations, and optimized structures for DFT calculations are provided in the Supplementary Information or are available online at https://github.com/AmanchukwuLab/water_activity_aprotic_CO2R_HER (ref. 69). The data supporting the findings of this study are available within the article and its Supplementary Information, or can be obtained from the corresponding author on reasonable request.

References

- McCrory, C. C. L., Jung, S., Peters, J. C. & Jaramillo, T. F. Benchmarking heterogeneous electrocatalysts for the oxygen evolution reaction. J. Am. Chem. Soc. 135, 16977–16987 (2013).
- Liang, Y. & Yao, Y. Designing modern aqueous batteries. Nat. Rev. Mater. 8, 109–122 (2022).
- 3. Li, J., Li, X., Gunathunge, C. M. & Waegele, M. M. Hydrogen bonding steers the product selectivity of electrocatalytic CO reduction. *Proc. Natl Acad. Sci. USA* **116**, 9220–9229 (2019).
- Birdja, Y. Y. et al. Advances and challenges in understanding the electrocatalytic conversion of carbon dioxide to fuels. *Nat. Energy* 4, 732–745 (2019).
- Velasco-Velez, J. J. et al. The structure of interfacial water on gold electrodes studied by X-ray absorption spectroscopy. Science 346, 831–834 (2014).

- Li, P. et al. Hydrogen bond network connectivity in the electric double layer dominates the kinetic pH effect in hydrogen electrocatalysis on Pt. Nat. Catal. 5, 900–911 (2022).
- Wang, Y. H. et al. In situ Raman spectroscopy reveals the structure and dissociation of interfacial water. Nature 600, 81–85 (2021).
- Li, C. Y. et al. In situ probing electrified interfacial water structures at atomically flat surfaces. Nat. Mater. 18, 697–701 (2019).
- Ledezma-Yanez, I. et al. Interfacial water reorganization as a pH-dependent descriptor of the hydrogen evolution rate on platinum electrodes. Nat. Energy 2, 17031 (2017).
- Suo, L. et al. "Water-in-salt" electrolyte enables high-voltage aqueous lithium-ion chemistries. Science 350, 938–943 (2015).
- Laage, D. & Stirnemann, G. Effect of ions on water dynamics in dilute and concentrated aqueous salt solutions. J. Phys. Chem. B 123, 3312–3324 (2019).
- 12. Chao, D. et al. Roadmap for advanced aqueous batteries: from design of materials to applications. Sci. Adv. 6, eaba4098 (2020).
- Xie, J., Liang, Z. & Lu, Y. C. Molecular crowding electrolytes for high-voltage aqueous batteries. Nat. Mater. 19, 1006–1011 (2020).
- 14. Wang, T. et al. Hydrogen-bond network manipulation of aqueous electrolytes with high-donor solvent additives for Al-air batteries. *Energy Storage Mater.* **45**, 24–32 (2022).
- Wang, Y. et al. Enabling high-energy-density aqueous batteries with hydrogen bond-anchored electrolytes. *Matter* 5, 162–179 (2022).
- Zhou, L. et al. Suppressing hydrogen evolution in aqueous lithium-ion batteries with double-site hydrogen bonding. ACS Energy Lett. 29, 40–47 (2022).
- Shin, H., Hansen, K. U. & Jiao, F. Techno-economic assessment of low-temperature carbon dioxide electrolysis. *Nat. Sustain* 4, 911–919 (2021).
- Verma, S., Kim, B., Jhong, H. R. M., Ma, S. & Kenis, P. J. A. A gross-margin model for defining technoeconomic benchmarks in the electroreduction of CO₂. Chem. Sus. Chem. 9, 1972–1979 (2016).
- Ikeda, S., Takagi, T. & Ito, K. Selective formation of formic acid, oxalic acid, and carbon monoxide by electrochemical reduction of carbon dioxide. *Bull. Chem. Soc. Jpn.* 60, 2517–2522 (1987).
- Tomita, Y., Teruya, S., Koga, O. & Hori, Y. Electrochemical reduction of carbon dioxide at a platinum electrode in acetonitrile-water mixtures. J. Electrochem. Soc. 147, 4164 (2000).
- Joshi, P. B., Karki, N. & Wilson, A. J. Electrocatalytic CO₂ reduction in acetonitrile enhanced by the local environment and mass transport of H₂O. ACS Energy Lett. 7, 602–609 (2022).
- Dubouis, N. et al. Tuning water reduction through controlled nanoconfinement within an organic liquid matrix. Nat. Catal. 3, 656–663 (2020).
- Figueiredo, M. C., Ledezma-Yanez, I. & Koper, M. T. M. In situ spectroscopic study of CO₂ electroreduction at copper electrodes in acetonitrile. ACS Catal. 6, 2382–2392 (2016).
- Kash, B., Gomes, R. & Amanchukwu, C. Mitigating electrode inactivation during CO₂ electrocatalysis in aprotic solvents with alkali cations. J. Phys. Chem. Lett. 14, 920–926 (2023).
- 25. Gomes, R. J. et al. Probing electrolyte influence on CO_2 reduction in aprotic solvents. *J. Phys. Chem. C.* **126**, 13595–13606 (2022).
- Rabinowitz, J. A. & Kanan, M. W. The future of low-temperature carbon dioxide electrolysis depends on solving one basic problem. *Nat. Commun.* 11, 5231 (2020).
- Huang, J. E. et al. CO₂ electrolysis to multicarbon products in strong acid. Science 372, 1074–1078 (2021).
- 28. Wernet, P. et al. The structure of the first coordination shell in liquid water. *Science* **304**, 995–999 (2004).

- Bakker, H. J. & Skinner, J. L. Vibrational spectroscopy as a probe of structure and dynamics in liquid water. *Chem. Rev.* 110, 1498–1517 (2010).
- Auer, B. M. & Skinner, J. L. Water: hydrogen bonding and vibrational spectroscopy, in the bulk liquid and at the liquid/vapor interface. *Chem. Phys. Lett.* 470, 13–20 (2009).
- Pribble, R. N. & Zwier, T. S. Size-specific infrared spectra of benzene-(H₂O)_n clusters (n = 1 through 7): evidence for noncyclic (H₂O)_n structures. Science 265, 75–79 (1994).
- 32. Yang, X. et al. Infrared spectroscopy of neutral water clusters at finite temperature: evidence for a noncyclic pentamer. *Proc. Natl Acad. Sci. USA* **117**, 15423–15428 (2000).
- Xantheas, S. S. & Dunning, T. H. Ab initio studies of cyclic water clusters (H₂O)_n, n = 1–6. I. Optimal structures and vibrational spectra. J. Chem. Phys. 99, 8774–8792 (1993).
- Huisken, F., Kaloudis, M. & Kulcke, A. Infrared spectroscopy of small size-selected water clusters. J. Chem. Phys. 104, 17–25 (1996).
- Scatena, L. F., Brown, M. G. & Richmond, G. L. Water at hydrophobic surfaces: weak hydrogen bonding and strong orientation effects. Science 292, 908–912 (2001).
- Ohno, K., Okimura, M., Akai, N. & Katsumoto, Y. The effect of cooperative hydrogen bonding on the OH stretching-band shift for water clusters studied by matrix-isolation infrared spectroscopy and density functional theory. *Phys. Chem. Chem. Phys.* 7, 3005–3014 (2005).
- Perera, P. N. et al. Observation of water dangling OH bonds around dissolved nonpolar groups. *Proc. Natl Acad. Sci. USA* 106, 12230–12234 (2009).
- Tomlinson-Phillips, J. et al. Structure and dynamics of water dangling OH bonds in hydrophobic hydration shells. Comparison of simulation and experiment. J. Phys. Chem. A 115, 6177–6183 (2011).
- Hsieh, C. S. et al. Ultrafast reorientation of dangling OH groups at the air-water interface using femtosecond vibrational spectroscopy. *Phys. Rev. Lett.* 107, 116102 (2011).
- Dereka, B., Lewis, N. H. C., Keim, J. H., Snyder, S. A. & Tokmakoff,
 A. Characterization of acetonitrile isotopologues as vibrational probes of electrolytes. J. Phys. Chem. B 126, 278–291 (2022).
- 41. Mikenda, W. Stretching frequency versus bond distance correlation of OD(H)...Y (Y N, O, S, Se, Cl, Br, I) hydrogen bonds in solid hydrates. *J. Mol. Struct.* **147**, 1–15 (1986).
- 42. Steiner, T. The hydrogen bond in the solid state. *Angew. Chem. Int. Ed.* 41, 48–76 (2002).
- 43. Zarycz, M. N. C. & Fonseca Guerra, C. NMR 1H-shielding constants of hydrogen-bond donor reflect manifestation of the Pauli principle. *J. Phys. Chem. Lett.* **9**, 3720–3724 (2018).
- 44. Rohlfing, C. M. M., Allen, L. C. & Ditchfield, R. Proton chemical shift tensors in hydrogen-bonded dimers of RCOOH and ROH. *J. Chem. Phys.* **79**, 4958–4966 (1998).
- Fawcett, W. R. Acidity and basicity scales for polar solvents.
 J. Phys. Chem. 97, 9540–9546 (1993).
- Jeffrey, G. A. An Introduction to Hydrogen Bonding (Oxford Univ. Press, 1997).
- Venkatraman, R. K. & Baiz, C. R. Ultrafast dynamics at the lipidwater interface: DMSO modulates H-bond lifetimes. *Langmuir* 36, 6502–6511 (2020).
- 48. Nicodemus, R. A., Corcelli, S. A., Skinner, J. L. & Tokmakoff, A. Collective hydrogen bond reorganization in water studied with temperature-dependent ultrafast infrared spectroscopy. *J. Phys. Chem. B* **115**, 5604–5616 (2011).
- Sarode, H. N. et al. Insights into the transport of aqueous quaternary ammonium cations: a combined experimental and computational Study. J. Phys. Chem. B 118, 1363–1372 (2014).

- Benck, J. D., Hellstern, T. R., Kibsgaard, J., Chakthranont, P. & Jaramillo, T. F. Catalyzing the hydrogen evolution reaction (HER) with molybdenum sulfide nanomaterials. ACS Catal. 4, 3957–3971 (2014).
- Murthy, A. P., Theerthagiri, J. & Madhavan, J. Insights on Tafel constant in the analysis of hydrogen evolution reaction. *J. Phys. Chem. C.* 122, 23943–23949 (2018).
- Rudnev, A. V. et al. The promoting effect of water on the electroreduction of CO₂ in acetonitrile. *Electrochim. Acta* 189, 38–44 (2016).
- Anouti, M., Dougassa, Y. R., Tessier, C., El Ouatani, L. & Jacquemin, J. Low pressure carbon dioxide solubility in pure electrolyte solvents for lithium-ion batteries as a function of temperature. Measurement and prediction. J. Chem. Thermodyn. 50, 71–79 (2012).
- Welford, P. J. et al. The electro-reduction of carbon dioxide in dimethyl sulfoxide at gold microdisk electrodes: current/voltage waveshape analysis. J. Phys. Chem. B 105, 5253–5261 (2001).
- 55. König, M., Vaes, J., Klemm, E. & Pant, D. Solvents and supporting electrolytes in the electrocatalytic reduction of CO₂. *iScience* **19**, 135–160 (2019).
- Zhang, Q. et al. Micro-electrode with fast mass transport for enhancing selectivity of carbonaceous products in electrochemical CO₂ reduction. Adv. Funct. Mater. 31, 2103966 (2021).
- Goyal, A., Marcandalli, G., Mints, V. A. & Koper, M. T. M. Competition between CO₂ reduction and hydrogen evolution on a gold electrode under well-defined mass transport conditions. J. Am. Chem. Soc. 142, 4154–4161 (2020).
- Ooka, H., Figueiredo, M. C. & Koper, M. T. M. Competition between hydrogen evolution and carbon dioxide reduction on copper electrodes in mildly acidic media. *Langmuir* 33, 9307–9313 (2017).
- Krishtalik, L. I. Kinetic isotope effect in the hydrogen evolution reaction. Electrochim. Acta 46, 2949–2960 (2001).
- 60. Fairley, N. et al. Systematic and collaborative approach to problem solving using X-ray photoelectron spectroscopy. *Appl Sur Sci. Adv.* **5**, 100112 (2021).
- 61. Won, D. H. et al. Highly efficient, selective, and stable CO_2 electroreduction on a hexagonal Zn catalyst. *Angew. Chem.* **128**, 9443–9446 (2016).
- Rosen, J. et al. Electrodeposited Zn dendrites with enhanced CO selectivity for electrocatalytic CO₂ reduction. ACS Catal. 5, 4586–4591 (2015).
- 63. Nguyen, D. L. T. et al. Selective CO₂ reduction on zinc electrocatalyst: the effect of zinc oxidation state induced by pretreatment environment. ACS Sustain Chem. Eng. **5**, 11377–11386 (2017).
- 64. Izutsu, K. Electrochemistry in Nonaqueous Solutions (Wiley, 2002).
- Plimpton, S. Fast parallel algorithms for short-range molecular dynamics. J. Comput. Phys. 117, 1–19 (1995).
- 66. Frisch, M. J. et al. Gaussian 16 (Gaussian, 2016).
- Giannozzi, P. et al. QUANTUM ESPRESSO: a modular and open-source software project for quantum simulations of materials. J. Phys: Condens. Matter 21, 395502 (2009).
- Murbach, M. D., Gerwe, B., Dawson-Elli, N. & Tsui, L. impedance. py: a Python package for electrochemical impedance analysis. J. Open Source Softw. 5, 2349 (2020).
- AmanchukwuLab/water_activity_aprotic_CO2R_HER. GitHub https://github.com/AmanchukwuLab/water_activity_aprotic_ CO2R_HER (2024).

Acknowledgements

This work was primarily supported by the U.S. Department of Energy Office of Science Basic Energy Sciences, Early Career Research Program (DE-SC0024103). C.V.A. was supported by the CIFAR Azrieli Global Scholars Program. R.J.G. was partially supported by the Roberto Rocca Scholars Program. R.K. was supported by the Eric and Wendy Schmidt AI in Science Postdoctoral Fellowship. H.F. was supported by the National Science Foundation Graduate Research Fellowship Program. I.R. was supported by the UChicago Quad Scholars Program. We thank N.H.C. Cohen and A. Tokmakoff for insightful discussions, and C. Vu for the scanning electron microscopy images. This work made use of the shared facilities (Raman) at the University of Chicago Materials Research Science and Engineering Center, supported by the National Science Foundation under award no. DMR-2011854. Fourier-transform infrared was performed at the Soft Matter Characterization Facility of the University of Chicago. Solution-state NMR measurements were performed at the UChicago Chemistry NMR Facility. Molecular dynamics and DFT calculations were performed with resources provided by the University of Chicago's Research Computing Center.

Author contributions

R.J.G. and C.V.A. conceptualized the paper. R.J.G. was responsible for the methodology and carried out the investigation. R.K. performed the MD and DFT calculations. H.F. performed experimental validation. I.R. performed NMR characterization. B.S. performed electrolyte stability analysis. R.J.G. and C.V.A. wrote the manuscript and all co-authors contributed to editing. C.V.A. supervised the work.

Competing interests

There authors declare no comepting interests.

Additional information

Supplementary information The online version contains supplementary material available at https://doi.org/10.1038/s41929-024-01162-z.

Correspondence and requests for materials should be addressed to Chibueze V. Amanchukwu.

Peer review information *Nature Catalysis* thanks the anonymous reviewers for their contribution to the peer review of this work.

Reprints and permissions information is available at www.nature.com/reprints.

Publisher's note Springer Nature remains neutral with regard to jurisdictional claims in published maps and institutional affiliations.

Springer Nature or its licensor (e.g. a society or other partner) holds exclusive rights to this article under a publishing agreement with the author(s) or other rightsholder(s); author self-archiving of the accepted manuscript version of this article is solely governed by the terms of such publishing agreement and applicable law.

@ The Author(s), under exclusive licence to Springer Nature Limited 2024